



NRL/MR/6410--03-8705

Simulation of Flow and Dispersion Around a Surface-Mounted Cube

SALLY A. CHEATHAM

*Center for Reactive Flow and Dynamical Systems
Laboratory for Computational Physics and Fluid Dynamics*

JAY P. BORIS

*Chief Scientist and Director
Laboratory for Computational Physics and Fluid Dynamics*

BOHDAN Z. CYBYK

*Center for Reactive Flow and Dynamical Systems
Laboratory for Computational Physics and Fluid Dynamics*

August 29, 2003

Approved for public release; distribution is unlimited.

20031010 046

REPORT DOCUMENTATION PAGE				<i>Form Approved</i> OMB No. 0704-0188	
Public reporting burden for this collection of information is estimated to average 1 hour per response, including the time for reviewing instructions, searching existing data sources, gathering and maintaining the data needed, and completing and reviewing this collection of information. Send comments regarding this burden estimate or any other aspect of this collection of information, including suggestions for reducing this burden to Department of Defense, Washington Headquarters Services, Directorate for Information Operations and Reports (0704-0188), 1215 Jefferson Davis Highway, Suite 1204, Arlington, VA 22202-4302. Respondents should be aware that notwithstanding any other provision of law, no person shall be subject to any penalty for failing to comply with a collection of information if it does not display a currently valid OMB control number. PLEASE DO NOT RETURN YOUR FORM TO THE ABOVE ADDRESS.					
1. REPORT DATE (DD-MM-YYYY) August 29, 2003		2. REPORT TYPE		3. DATES COVERED (From - To)	
4. TITLE AND SUBTITLE Simulation of Flow and Dispersion Around a Surface-Mounted Cube				5a. CONTRACT NUMBER	
				5b. GRANT NUMBER 64-1528-03	
				5c. PROGRAM ELEMENT NUMBER	
6. AUTHOR(S) Sally A. Cheatham, Jay Boris, and Bohdan Z. Cybyk,*				5d. PROJECT NUMBER	
				5e. TASK NUMBER	
				5f. WORK UNIT NUMBER	
7. PERFORMING ORGANIZATION NAME(S) AND ADDRESS(ES) Naval Research Laboratory, Code 6410 4555 Overlook Avenue, SW Washington, DC 20375-5320				8. PERFORMING ORGANIZATION REPORT NUMBER NRL/MR/6410--03-8705	
9. SPONSORING / MONITORING AGENCY NAME(S) AND ADDRESS(ES)				10. SPONSOR / MONITOR'S ACRONYM(S)	
				11. SPONSOR / MONITOR'S REPORT NUMBER(S)	
12. DISTRIBUTION / AVAILABILITY STATEMENT Approved for public release; distribution is unlimited.					
13. SUPPLEMENTARY NOTES *Currently with Johns Hopkins University, Applied Physics Laboratory, Laurel, MD					
14. ABSTRACT The time-accurate computational model FAST3D is used to investigate flow over a cube mounted on a flat surface. The effect of resolution, boundary conditions, and the form of the inflow velocity profile on flow evolution and passive tracer dispersion in the vicinity of the cube is considered. Computational results are compared with wind tunnel and water tank data published by a number of authors. It is found that the flow computed around a surface-mounted cube is sensitive to both the form of the upstream velocity profile as well as to conditions at the baseplate surface. Furthermore, time-dependent effects appear to be crucial to the accumulation of accurate flow field statistics and thus a correct understanding of the flow and dispersion patterns.					
15. SUBJECT TERMS Large eddy simulation; Surface-mounted cube; Contaminant dispersion					
16. SECURITY CLASSIFICATION OF:			17. LIMITATION OF ABSTRACT UL	18. NUMBER OF PAGES 26	19a. NAME OF RESPONSIBLE PERSON Sally A. Cheatham
a. REPORT Unclassified	b. ABSTRACT Unclassified	c. THIS PAGE Unclassified			19b. TELEPHONE NUMBER (include area code) (202) 767-0525

CONTENTS

1. INTRODUCTION	1
2. CALIBRATION, VALIDATION, AND RESEARCH	1
3. BACKGROUND	1
4. GOVERNING EQUATIONS	3
5. COMPUTATIONAL RESULTS FOR THE BASELINE CASE.....	3
6. NUMERICAL RESOLUTION	4
7. EFFECT OF MOMENTUM-DEFICIT BOUNDARY CONDITION	5
8. VARIATION OF THE INFLOW VELOCITY PROFILE	6
9. COMBINED EFFECT OF INITIAL AND BOUNDARY CONDITIONS	7
10. DISCUSSION	8
11. CONCLUSIONS	10
12. ACKNOWLEDGMENTS	10
13. REFERENCES	10

SIMULATION OF FLOW AND DISPERSION AROUND A SURFACE-MOUNTED CUBE

1. INTRODUCTION

This work describes fluid dynamics studies using NRL's FAST3D-CT (Contaminant Transport) model directly relevant to the accurate simulation of the transport and dispersion of contaminants and passive tracers external to buildings in urban settings. The focal configuration is flow over a surface-mounted cube. Fluid dynamics can become arbitrarily complex in even such a simple flow geometry when turbulence is present. Therefore, since the cube is a single parameter representation (i.e. size) that approximates many buildings, it is an excellent test problem for urban contaminant transport simulations. The study is validated by wind tunnel and water tank data published by a number of authors (Snyder 1994, Castro and Robins 1977.) The extensibility of the results depends on the simulation model's ability to represent more complex geometries and realistic inflow conditions easily and faithfully.

The effect of resolution, boundary conditions, and the form of the inflow velocity profile on flow evolution and passive tracer dispersion in the vicinity of the cube is considered. It is found that the flow computed around a surface-mounted cube is sensitive to both the form of the upstream velocity profile as well as to conditions at the baseplate surface. Furthermore, time-dependent effects appear to be crucial to the accumulation of accurate flow field statistics and thus a correct understanding of the flow and dispersion patterns.

2. CALIBRATION, VALIDATION, AND RESEARCH

For external CT applications, as well as many other real-world uses of detailed modeling, the notion of "model validation" should encompass what we really do and really need to do. Modelers really engage in a three-stage process that is better described as staged calibration. The first stage is experimental with computational interpretation – the determination of the appropriate model input. Here *input* means not only the initial conditions but also includes the continuously updated boundary conditions that describe atmospheric variations in external scenarios and changes to the HVAC settings, sources, sinks, and openings/leaks in interior scenarios. The second stage is computational, the use of a numerical model to simulate a solution based on the input. The third stage is again both experimental and computational, the interpretation and comparison of the experimental and computational results.

Validation is an ongoing process where the range of applicability of a model is being gradually widened and the understanding of a model's limitations and the reliable accuracy of its forecasts is being accordingly increased. Since validation, as an achievable end state, is largely a figment of the imagination, a model should be used in a balanced way to develop useful new information even as ongoing calibration and validation are being performed. In the area of external contaminant transport, the overall situation is made worse by the fact that experiments are not easily controlled, not repeatable, and generally poorly characterized. An essential feature of validation is a thorough understanding of the inflow conditions, and the reliability/repeatability of experimental results. Therefore, wind tunnel and water tank experiments are really the only place where satisfactory validation, in the strictest sense, can be performed.

3. BACKGROUND

A number of experimental and numerical studies of the surface-mounted cube have been conducted and reported in the literature. Qualitative features of the flow have been described by Martinuzzi and Tropea (1993) and by Hunt et al. (1978). A major feature of the flow is a time-averaged horseshoe vortex, originating near the upwind face of the cube, whose arms extend downstream on each side of the cube. Other noteworthy characteristics include separation stream lines in front of the cube, a recirculation bubble on the cube top, as well as a closed-arch vortex immediately downstream of the cube (for a schematic, see Martinuzzi and Tropea (1993).) These are time-averaged features upon which complex, time-dependent vortex shedding events are superimposed.

Experimental measurements of the flow include those reported in Snyder (1994), Castro and Robins (1977), and Lakehal and Rodi (1997). Of primary interest for CT applications are the passive tracer concentration measurements of Snyder (Snyder 1994, Zhang et al. 1996). In his towing tank experiments, a dye source was placed to the lee side of a surface-mounted cube, at the baseplate surface. Dye concentration measurements were taken at the surface centerline to $6.5H$ downstream of the cube center, where H is the cube height. Lateral concentration profiles at the baseplate surface as well as concentration profiles vertical to the surface at the centerline were measured. The same cubical building model was used in wind tunnel experiments to examine how characteristics of the approach flow might change the concentration profiles; here ethane gas was released as a tracer. Useful flow field measurements

are also found in the work of Castro and Robins (1977), who performed experiments investigating air flow over a surface-mounted cube in a wind tunnel. In their work, both uniform, and sheared turbulent, inlet flow are discussed. Their results include mean velocity profiles at several lateral and vertical locations as well as pressure coefficient data. The work of Martinuzzi and Tropea (1993) provides results for flow around other surface-mounted objects in fully developed channel flow. Results from both a water and air channel are described. Particular attention is devoted to the separation region in front of the cube. The reattachment region behind the cube is also discussed. A similar study with additional results is found in the work by Larousse, Martinuzzi and Tropea (1993). Here, time-averaged velocity vectors are presented, as well as information on separation and reattachment patterns and flow visualization results.

There have also been several numerical studies of flow around a cube. Zhang et al. (1996) used the $k - \epsilon$ model TEMPEST to simulate flow over a surface-mounted cube. A source is introduced at the surface behind the cube in their calculation, so that concentration profiles downstream may be obtained and compared with the data of Snyder (1994). Averaged velocity vector plots and reattachment lengths are also discussed, particularly with respect to their variation with the Froude number. In another work, Zhang and coworkers (1993) used the TEMPEST $k - \epsilon$ model to investigate the effects of incident shear and turbulence on the flow around a cube. Averaged velocity fields are compared with the experimental data of Castro and Robins (1977). Lakehal and Rodi (1997) numerically investigated the flow field surrounding a cube in developed channel flow. Their 3D steady calculations used various $k - \epsilon$ turbulence models. Results are compared with the experimental measurements of Martinuzzi and Tropea (1993). Werner and Wengle (1993) numerically calculated the flow over and around a surface-mounted cube in a channel using a large-eddy simulation (LES) method. Their results include instantaneous and time-averaged velocity profiles. Vorticity and mean recirculation lengths are also discussed. Chan et al. (2000) used a finite element model to study flow and dispersion around a cube. Their study compares results from both LES and nonlinear eddy viscosity (NEV) calculations to experimental data. They conclude that LES yields better agreement with experiments than NEV, but at a higher computational cost. Numerical simulations of fully developed channel flow over a cube by several research groups are described by Rodi et al. (1997) in their summary of results from a workshop on LES flows over blunt bodies. Shah (1998) investigates large eddy simulations of flow past a surface-mounted cube in channel flow. Additional numerical studies have focused on application to atmospheric boundary layer flows and have investigated flow past a cube in turbulent boundary layers of characteristic height several times that of the cube. Such studies include those of Paterson and Apelt (1990), and Murakami et al. (1992). Hunt et al. (1978) provide an interesting theoretical study based on topology to predict qualitative characteristics of the flow around a surface-mounted cube. Kinematical principles are used in discussing flow patterns via singular points of the shear stress and mean velocity.

The present study investigates why LES models appear to do better than turbulence-averaged approaches and presents results to demonstrate the physical sensitivity to several important input conditions and physical approximations. The attraction of these turbulence-averaged models is the potential for shorter computations to find a converged steady-state flow field, as opposed to computing the extensive evolution of a flow field using a time-accurate method. In the case of a cube, furthermore, a steady-state approximation should have a symmetry plane, reducing the required computation further. Turbulence averaged-models include both those built on the assumption of a steady-average state, and those unsteady models in which the resolvable turbulence field is still averaged in some way, even if the "average" state can vary slowly in principle.

The problem appears to arise in these models because the averaging is performed before the nonlinear flow field is computed rather than afterward (see Oran and Boris, 2001). The approximations typically made suppress the shedding of vortices of cube (building) scale. It is this unsteady shedding process that actually accounts for much of the tracer dispersion. Because this dispersion is intrinsically convective in nature on the resolved scales, it is poorly approximated by diffusion terms, no matter how complex. Furthermore, turbulence-averaging approximations are typically non-convergent in the following sense. The averaging performed on the fluid equations makes its largest errors at the scales where the fluctuating turbulence field has the most energy and varies on time scales at least as long as other dynamic, convective time scales in the system. These scales are well resolved spatially and thus the errors impressed on the solution by these apparently simplifying mathematical approximations are not made smaller as the grid scale is improved. The computed solutions cannot converge as the grid is refined to the underlying solutions of the appropriate Navier-Stokes equations. By way of contrast, Ikeda and Nakagawa (1979) have shown that the forerunner algorithm to FAST3D converges to the correct solution of the underlying continuity equations.

In practice, giving up convergence of the turbulence-averaged solutions does not actually seem to buy much in

performance. The fluid dynamics typically “knows” that it should be unsteady so convergence of turbulence-averaged models is correspondingly slow. Furthermore, solution of steady-state models in complex geometry is usually quite expensive. As a result, supercomputers and parallel processors are still required for quick solutions, a situation generally exacerbated by the added expense of finite-element modeling approaches. By way of comparison, extensive three-dimensional urban computations using FAST3D (e.g. in $1.5 \text{ km} \times 1.5 \text{ km}$ domains to 300 meter altitude to five meter resolution) can be performed in a few hours on modest multiprocessors and in a couple of days on single-processor MacIntosh desktop computers and portables.

4. GOVERNING EQUATIONS

In the present work we use the FAST3D model to investigate flow over a surface-mounted cube. FAST3D solves three-dimensional, time-dependent, compressible reactive flow problems. The underlying fluid convection algorithm is the Flux-Corrected Transport (FCT) algorithm (Boris and Book, 1973, 1976 and Boris et al. 1993). This is a high-resolution, direction-split, monotone, conservative, positivity-preserving convective algorithm.

The governing equations we solve are the conservative continuity equations in the limit of large Reynolds number

$$\frac{\partial \rho}{\partial t} = -\nabla \cdot \rho \mathbf{v} \quad (1)$$

$$\frac{\partial \rho \mathbf{v}}{\partial t} = -\nabla \cdot \rho \mathbf{v} \mathbf{v} - \nabla P \quad (2)$$

$$\frac{\partial E}{\partial t} = -\nabla \cdot E \mathbf{v} - \nabla \cdot \mathbf{v} P \quad (3)$$

where ρ is the density, $\mathbf{v} = (v_x, v_y, v_z)$ is the velocity, P is the pressure, and E the total energy density. These equations are solved together with the continuity equations describing the time evolution of a number of chemical species densities c treated as passive contaminant tracers

$$\frac{\partial c}{\partial t} = -\nabla \cdot c \mathbf{v}. \quad (4)$$

In the computations, a tracer chemical species source is located a distance approximately $H/4$ from the back edge of the cube at the baseplate, and lying on the longitudinal centerline. This “contaminant” is added to the flow field at each timestep, at a constant rate. In presenting results, the tracer species density is normalized to facilitate comparison with experiments and other numerical results. In the following, normalized concentration χ is defined as $\chi = CUH^2/Q$, where C is the dimensional tracer species density, U is the incoming characteristic flow velocity, H is the cube height and Q is the source flow rate in g/s . Solutions are computed at cell-centers for all variables. In the following, $y \sim 0$, for example, refers to data at the cell center above $y = 0$, that is, at $y = 0.5 \text{ m}$ if the discretization size $\Delta y = 1 \text{ m}$. Ambient density was taken to be that of air, $\rho_{amb} = 1.226 \times 10^{-3} \text{ g cm}^{-3}$, and the ambient pressure was scaled as $P_{amb} = 2.5331 \times 10^3 \text{ erg cm}^{-3}$ to simulate a flow of Mach number $Ma \sim 0.176$ when the ambient velocity is 3 m s^{-1} (this is a pseudo-compressibility model.) Turbulence in the system is modeled through the Large Eddy Simulation method MILES (Boris et al., 1992). In this approach, subgrid effects are accounted for directly by the non-linear flux limiting of the convection algorithm, instead of through added terms in the system of equations. Analyses by Fureby and Grinstein (1999, 2000, 2002) have shown MILES to be a computationally efficient approach to turbulence modeling which correctly replicates the anisotropic nature of eddy transport.

5. COMPUTATIONAL RESULTS FOR THE BASELINE CASE

One particular configuration was chosen as the baseline case. Parameter excursions were then computed to understand the important physical and numerical factors influencing the evolution of the fluid dynamics. For our baseline case, we have chosen a cube height H of 16 m . The grid size in this base simulation is $176 \times 56 \times 120$ cells ($\ell \times h \times w$). The grid has been stretched at the edges to move the boundaries of the domain far from the region of interest. The domain, as a result, is approximately $18H \times 3.5H \times 8.5H$ in extent. In the unstretched region, the cell size is 1 m in each direction. The cube center is located approximately $5H$ from the inlet plane, at $x = 0, y = 0, z = 0.5H = 8 \text{ m}$, so the back face of the cube corresponds to $x = 0.5H$. The incoming velocity is assumed laminar and uniform at 3 m s^{-1} in the baseline case, and an outflow condition is imposed at the exit plane. Here we note explicitly that our

study is designed for comparison to experiments with a uniform, non-turbulent inflow, specifically the experiments of Castro and Robins (1977, Case A) and Snyder (1994). A momentum drag boundary condition, discussed in more detail in Section 7, was applied on the base plate and at the cube surface, while an open flow condition was prescribed at the top. An ideal solid wall condition was applied at the lateral walls of the computational domain.

The calculation was run for 95,000 timesteps. Time-averages were computed by taking data at every 100th timestep between steps 15,000 and 95,000. Averaging began at timestep 15,000 in order to allow initial transients time to decay. For the baseline case, the timestep was fixed at $dt = .01 s$, which corresponds to $CFL \sim 0.2$.

Results for the baseline case are shown in Figures 1-3. In Figure 1, averaged and instantaneous contours of the three velocity components and the concentration field are shown at the baseplate in a view from the top. The instantaneous contours were taken at timestep 55,000. Contours of v_x correspond to the range $(-3 m s^{-1}, 3 m s^{-1})$. For v_y and v_z the contours represent $(-0.3 m s^{-1}, 0.3 m s^{-1})$ to better elucidate features of the flow field. The midpoint contour corresponds to the color black. Therefore black regions in the velocity contours correspond to a velocity near zero. These flow visualizations give good insight into the small scales allowed in this LES model and the importance of variability and time accuracy.

In Figure 1, contours of average v_y and v_z display the existence of a horseshoe vortex. The v_x contour shows the recirculation regions in front of and behind the cube. We calculate a front recirculation length of $R_F = 0.94H$ and a recirculation length at the back of the cube of length $R_R = 2.52H$, based on where the average v_x changes signs at the baseplate longitudinal centerline. The contours of instantaneous concentration illustrate the time-dependent vortex shedding off the back of the cube. In Figure 2, a side view of contours of velocity components and concentration are shown near the centerline $z = 0$. Here again the recirculation regions in front of and behind the cube are clearly visible, as is a recirculation region on the cube top. More details of the flow patterns appear in Figure 3, where spanwise cross-sections at $x = H$ (half a cube length from the back edge of the cube) are shown. The outline of the cube from upstream is projected onto the contours. The lateral cross sections at $x = H$, particularly as demonstrated by contours of average v_x and concentration, appear to have a slightly hexagonal shape. Contours of average v_y and v_z in the figure suggest the arms of the horseshoe vortex are well-defined at this downstream location, and are centered vertically close to the baseplate, below $y = 0.5H$.

6. NUMERICAL RESOLUTION

The effect of grid resolution on the features of the flow field was considered to determine the grid size needed to accurately resolve the flow. To this end, discretization of the cube and flow field were correspondingly altered to investigate cube sizes of $N_H = 6, 8, 12, 24$ and 32 cells. In the following, unless otherwise specified, all quantities are time-averaged from timesteps 15,000-95,000 with data taken every 100th timestep. The timestep Δt was altered with the discretization to maintain a CFL number $CFL \sim 0.2$. All other modeling inputs and boundary conditions are consistent with the baseline case previously discussed.

Typical resolution study results are shown in Figure 4. Here profiles of average velocity v_x versus y/H (vertical to the baseplate) are shown at $x = H$, for several resolutions. The experimental data are from Castro and Robins (1977). While all cube sizes show general agreement with the experimental data, as the resolution increases solutions more closely approach the experimental results. In particular, cube sizes of $N_H = 12, 16, 24$ and 32 give negative v_x velocities near the baseplate comparable to the experimental results, while resolutions of $N_H = 8$ and $N_H = 6$ give velocities near the base plate which are positive or zero, but then become negative further off the floor. Results for $N_H = 24$ and $N_H = 32$ are nearly identical and show good agreement with the experimental data, suggesting that these discretizations suffice to resolve the flow field. We note that $N_H = 16$ (the baseline resolution) gives similar results to these two resolutions, particularly several cube lengths downstream, with a noticeably smaller computational cost.

Variation of recirculation lengths in front of and behind the cube with respect to resolution have been calculated based on where the average v_x changes its sign at the base plate along the centerline $z \sim 0$. We find general trends that the recirculation region in front of the cube shrinks, and the reattachment length behind the cube becomes larger, as the resolution decreases. For cubes of $N_H = 6$ and $N_H = 8$ cells, there was essentially no recirculation region in front of the cube. Contour plots indicate that a stagnation point on the front face of the cube remains in these cases, but that instead of recirculating, the flow which is forced down towards the baseplate moves around the sides of the cube. As the resolution increases to $N_H = 12, 16, 24$, and 32 cells per cube height, the front recircula-

tion length R_F increases and begins to converge as R_F changes to $0.9H$, $0.93H$, $2.4H$, $2.84H$ respectively. Conversely, the recirculation zone behind the cube decreases in length as the resolution is increased, changing to $R_R = 6.75H$, $4.56H$, $2.63H$, $2.53H$, $2.2H$, $2.18H$ as the resolution is increased from $N_H = 6$ to $N_H = 8, 12, 16$, and 24 cells, respectively.

In Figure 5 normalized concentration along the centerline $z \sim 0$ at the baseplate $y \sim 0$ is shown. Here all resolutions show reasonable agreement with the experimental data far downstream of the cube. As the downstream distance decreases, calculations for the higher resolutions $N_H = 16, 24$ and $N_H = 32$ show the best agreement with the data.

7. EFFECT OF MOMENTUM-DEFICIT BOUNDARY CONDITION

In the above, a momentum deficit boundary condition was used at the base plate and cube surface to model the effect of unresolved viscous drag. Work is currently underway to extend and calibrate this model of an unresolved boundary layer. In the current implementation of such a boundary condition, drag is modeled by subtracting a percentage of the momentum at prescribed surfaces as

$$\rho \mathbf{v} = (1 - \epsilon)(\rho \mathbf{v})_{old}. \quad (5)$$

Thus $\epsilon = .0002$, for example, corresponds to subtracting .02% of the momentum, in each coordinate direction every timestep. Such a boundary condition can be used to implement and understand the effect of surface roughness on the flow field. Here ϵ can be thought of as a roughness parameter, with increasing ϵ approximating increasingly rough solid surfaces. We examine the effect of the magnitude of ϵ on the flow field, by varying ϵ from $\epsilon = 0$ (no drag) to $\epsilon = .00005, .0002, .0008$. The above condition (5) can also be written in terms of momentum loss due to surface friction with a corresponding drag coefficient c_d , as $\rho \mathbf{v} = (1.0 - c_d v^* dt/dx) \rho \mathbf{v}_{old}$ with v^* the magnitude of tangential velocity at the plate. When v^* equals its inflow value $v^* = 3m/sec$, the above values of ϵ are equivalent to $c_d = 0, .00167, .0066, .02667$ respectively. According to Tennekes and Lumley (1972), these are appropriate, reasonable values for drag coefficients. As in the baseline case, we use a cube size of $N_H = 16$ cells and a $3 m s^{-1}$ uniform inflow velocity profile.

Qualitatively, we find that as ϵ is decreased, the recirculation region in front of the cube decreases in size, with $\epsilon = 0$ corresponding to the limit of no recirculation. At the same time, the horseshoe vortex downstream of the cube becomes wider and more intense as ϵ is decreased. The average tracer-species concentration also changes with ϵ . Contours along the centerline $z \sim 0$ suggest that for the largest drag value $\epsilon = .0008$, the contaminant is more clustered behind the cube, while for $\epsilon = 0$ the contaminant is spread further downstream. Once the concentration begins to decrease, the $\epsilon = 0$ case has a faster decay rate in the downstream direction than cases with larger values of ϵ . This suggests that for $\epsilon = 0$ there may be more spreading in the lateral direction. Figure 6 shows that this is indeed the case. Here concentration at the baseplate is seen to be higher both laterally and downstream of the cube as ϵ is decreased. Contours of v_z at the baseplate also shown in Figure 6 help explain this result. As ϵ is decreased, the horseshoe vortex downstream becomes wider and more intense. It is reasonable to believe that the strong, coherent horseshoe vortex facilitates movement of the contaminant downstream and laterally in the domain. Note that for $\epsilon = 0$, there appears to be a break in the horseshoe about one cube height downstream from the back edge of the cube. This perhaps should rather be described as the start of the horseshoe vortex. For $\epsilon = 0$ there is no recirculation at the front cube face and so the front portion of the horseshoe does not have a vortical structure. Although there is a front recirculation zone for $\epsilon = .0008$, Figure 6 suggests that for strong damping there may also be an interruption of the horseshoe vortex just downstream of the cube, as well as a damping out of the horseshoe tails further downstream. In summary we find that a moderate value of ϵ is needed for a full horseshoe vortex. If ϵ is too small, there is no recirculation in front of the cube because the stagnation pressure maximizes at the cube-baseplate juncture. Thus the front of the horseshoe vortex will be missing. If ϵ is too large, just behind the cube there may be breaks in the horseshoe due to excessive slowing of the surface flow while further downstream the trailing tails of the horseshoe eventually cease to exist. These results are completely consistent with the expected fluid dynamic response to the input parameters.

Quantitative flow field results are shown in Figures 7-8. In Figure 7 normalized concentration at $x \sim 6.5H$, $z \sim 0$ is compared with the experimental data of Snyder (Zhang et al. 1996). Here data corresponding to $\epsilon = 0$ shows good agreement with the experimental data range, while results for non-zero ϵ are largely comparable and fall within the experimental range only near the baseplate. In Figure 8 the average velocity component v_y is shown at $x \sim 6.5H$,

$y \sim H$ along with experimental data from Castro and Robins (1977). Here too agreement between the numerical and experimental results is better for smaller values of ϵ . Front and rear circulation lengths have also been calculated to determine their dependence on ϵ . We find that recirculation lengths in front of the cube increase with increasing ϵ , from $R_F = 0$ for $\epsilon = 0$ to $R_F = .35H, .94H, 1.65H$ as ϵ is increased through $\epsilon = .00005, .0002, .0008$ respectively. Rear recirculation lengths change as $R_R = 2.65H, 2.8H, 2.52H, 2.56H$ as ϵ increases from $\epsilon = 0$ though $\epsilon = .0008$. Please note that these results were computed for a uniform (spatially constant) inflow velocity with no imposed temporal fluctuations.

8. VARIATION OF THE INFLOW VELOCITY PROFILE

In the above section, we saw that the parameter ϵ may be used to model momentum drag at solid surfaces, and that for a given value of ϵ , computed flow results show greater or lesser agreement with experiments depending on the region of the flow field of interest. For example, while several cube heights downstream results for $\epsilon = 0$ appear to most closely match the experimental results, in front of the cube non-zero values of ϵ result in better agreement with experiments. Therefore, to further investigate appropriate input parameters for realistically modeling the flow, we consider the effect of a non-uniform (but time-steady) inflow velocity profile. The intention here is to simulate the effect of viscous drag far upstream of the cube using a velocity profile which takes the existence of this upstream boundary layer into account. This should be an improvement over leaving the development of a boundary layer at the plate surface entirely to the momentum deficit boundary condition.

In the following, boundary layer-type profiles of the form

$$v_x = v_{x_{max}} - (v_{x_{max}} - v_{x_{min}}) \exp(-a * y) \quad (6)$$

are prescribed at the inflow, where a is the parameter varied among runs to control the boundary layer thickness. In the following, the smallest boundary layer thickness Case A corresponds to $a = 1.4$, (such that 99% of the freestream velocity $3m/s$ is reached at a vertical height of approximately $z_{bl} = 0.2H$) Case B to $a = 0.4$ ($z_{bl} = 0.7H$) and the largest boundary layer thickness Case C to $a = 0.2$ ($z_{bl} = 1.4H$). Initial flow velocity away from the plate $v_{x_{max}} = 3m/s$, and near the base plate $v_{x_{min}} = 0.5m/s$. In all flow initializations $v_y = v_z = 0.0m/s$. Again, the motivation behind this ad-hoc non-uniform but steady inflow profile is to model the effect of baseplate surface drag or roughness on the velocity field upstream of the cube and to understand the effect of an appreciable boundary layer thickness on flow and dispersion patterns. Consequently, in the following inflow profile runs, an ideal free-slip ($\epsilon = 0$) boundary condition is applied at the baseplate. A momentum deficit boundary condition is retained at the cube surface, since the effect of drag due to the cube cannot be modeled through the inflow conditions. In all runs, flow field dimensions correspond to those of the baseline case in which the cube height is $N_H = 16$ cells.

Calculations show that, as the boundary layer thickness increases, the recirculation region in front of the cube *increases* in length, while the recirculation region behind the cube *decreases* in length. These dependences are exactly as expected fluid dynamically. The separation streamline/stagnation point on the front face of the cube moves higher towards the cube top and the front recirculation region increases in size as the boundary layer thickness increases. All three boundary layer thicknesses result in recirculation regions on top of the cube, so that as in the baseline case, the flow is not attached on the cube top. This region appears to be slightly larger for the smallest boundary layer thickness, Case A. In the rear recirculation region, the average vertical velocity v_y becomes more strongly negative as the boundary layer thickness decreases. For the smallest inflow boundary layer thickness, Case A, the contaminant dispersion pattern near the back of the cube is wider than that for Cases B and C, but narrower further downstream. Case A inflow also results in a larger region of evenly distributed contaminant near the back of the cube than those found for Cases B and C. This is likely due to the larger v_y velocities in the rear recirculation zone for Case A. These result in a stronger rear recirculation region and thus greater mixing results. Calculations also suggest that a thick boundary layer expedites spreading of the contaminant downstream of the cube at the ground (or at least it moves away more slowly while spreading laterally.)

For non-uniform inflow, v_x along the baseplate longitudinal centerline can again be used to calculate recirculation lengths. As the boundary layer thickness increases, the length from the front face of the cube to the point where v_x changes sign increases, from $R_F = .37H$ for the smallest boundary layer thickness Case A to $R_F = .96H$ and $1.13H$ for Cases B and C. The reattachment length behind the cube decreases from $R_R = 2.59H$ for Case A to $R_R = 1.84H$ for Case B and $R_R = 1.71$ for the largest boundary layer thickness treated Case C. Additional quantitative results are

shown in Figure 9. Here calculations of average velocity v_x vertical to the baseplate at $x \sim H$, $z \sim 0$ show some agreement with the experiments of Castro and Robins (1977) for all three boundary layer thicknesses. The results from each numerical case alternately best match the experimental data in subsets of the domain. Lateral profiles of velocity at $x \sim 2H$ and $x \sim 6.5H$ suggest that Case A shows the best agreement with the experimental data, followed by Case B and then Case C.

Conversely, spanwise concentration profiles lateral on the baseplate at $x \sim 6.5H$ downstream are wider and agree slightly better with the experimental concentration data for the largest boundary layer thickness Case C. However, along the longitudinal centerline at $y \sim 0$, $z \sim 0$, concentration results for Case A show the best agreement with Snyder's experimental data. In Figure 10 one additionally sees that Case B falls partially within the experimentally reported range, and that Case C concentration results fall furthest from the experimental range.

While there is no definitive correlation between boundary layer thickness and agreement with experimental results, we may more generally conclude that use of a non-uniform inflow velocity profile results in fully formed horseshoe vortices both upstream and downstream of the cube, with front and rear recirculation lengths which depend on the inflow boundary layer thickness in a comprehensible way. More details distinguishing flow structure results for non-uniform inflow are discussed below.

9. COMBINED EFFECT OF INITIAL AND BOUNDARY CONDITIONS

Having examined the effects of a momentum deficit surface boundary condition and of a non-uniform inflow velocity profile separately, we examine the combined effect variations of these input parameters have on the flow field. Here we will consider together the permutations of 1) Case B inflow, $\epsilon = 0$ on the baseplate and the cube; 2) Case B inflow, $\epsilon = 0$ on the baseplate, $\epsilon = .0002$ on the cube; 3) Case B inflow, $\epsilon = .0002$ on the baseplate and the cube; 4) Uniform inflow, $\epsilon = 0$ on the baseplate and cube; 5) Uniform inflow, $\epsilon = .0002$ on the baseplate and cube. Comparisons are primarily used to determine the effect of a non-zero value of ϵ in combination with a non-uniform velocity inflow; uniform flow results were given above and are included here simply for ease of comparison. Again, we consider the baseline grid and resolution with $N_H = 16$ cells.

Contour shading plots of average v_y at $y \sim 0.5H$ for four of these cases are shown in top view in Figure 11. We see that a smoother, fuller horseshoe vortex results when a non-uniform inflow velocity profile is specified, and that one effect of ϵ is to dampen the intensity and reduce the size of the horseshoe vortex downstream of the cube. The combined effect of $\epsilon = .0002$ on the plate and cube surfaces and the Case B inflow profile is to produce a horseshoe vortex which is large in size upstream of the cube, while resulting in narrower, less intense arms of the horseshoe downstream as compared to results for Case B, $\epsilon = 0$.

Calculations of average velocities v_y and v_z at $x \sim 6.5H$ suggest that, as ϵ is increased, the horseshoe vortex is damped. Here it is interesting to compare results for non-uniform versus uniform inflow. For uniform inflow and $\epsilon = 0$, the arms of the horseshoe vortex remain intense and fairly near the lateral domain center. For non-uniform flow, however, the arms of the horseshoe vortex, while still strong, are significantly further apart, and are closer to the baseplate. However, for non-uniform inflow there also appears to be a much weaker vortex in a location comparable to that seen for uniform flow. These differences in the horseshoe vortex caused by the different inflow velocity conditions are depicted in Figures 12 and 13. Here average spanwise velocity v_z at $x \sim 6.5H$ downstream is shown at $y \sim H$ and at $y \sim 0.5H$, respectively. In Figure 12, uniform inflow with $\epsilon = 0$ comes closest to matching the experimental results of Castro and Robins. The maximum/minimum deviation from zero of the velocity v_z corresponds to the strongest points of the horseshoe vortex in this subsection of the domain. In Figure 13, we see a similar qualitative behavior of averaged v_z , but here the maximum and minimum are much further apart, corresponding to a wider horseshoe vortex. In Figure 13 this coherent structure is seen for *non-uniform* inflow with $\epsilon = 0$ on the baseplate, as opposed to the similar uniform flow result in Figure 12.

Figure 14 displays average velocity v_x along the baseplate longitudinal centerline $y \sim 0$, $z \sim 0$. For Case B inflow profiles, non-zero ϵ on the *cube* surface appears to have a negligible effect on the flow field upstream of the cube. However, behind the cube, non-zero ϵ has a noticeable effect on the flow structure, shortening the recirculation region and resulting in more strongly negative velocity v_x at the baseplate. As we have seen previously, an increase in ϵ on the baseplate lengthens the recirculation region in front of the cube. Downstream recirculation trends depend both on the value of ϵ on the cube surface and on the value of ϵ at the baseplate. In Figure 14, recirculation lengths for Case B inflow, with $\epsilon = .0002$ on the cube and $\epsilon = 0$ on the baseplate ($R_F = 0.97H$, $R_R = 1.84H$), best match

the experimental data of Martinuzzi and Tropea, who report a front recirculation length of $R_F = 1.04H$ and a rear recirculation length of $R_R = 1.6H$. Figure 15 shows averaged v_x at $x \sim 2H, y \sim H$. We again see that Case B inflow with $\epsilon = .0002$ on the cube and $\epsilon = 0$ on the plate again shows the best agreement with experiments, of Castro and Robins (1977). However, calculations show that further downstream uniform inflow with $\epsilon = 0$ best matches data of Castro and Robins. Finally, average concentration lateral to the baseplate at $x \sim 6.5H, y \sim 0$ are shown in Figure 16. Here best agreement between numerical calculations and experimental data is found when $\epsilon = 0$ on the baseplate, regardless of the structure of the inflow velocity profile.

More generally, we see that at $x \sim 6.5H$, best agreement with experimental results is obtained when $\epsilon = 0$ on the baseplate. At this downstream distance, the effect of a momentum deficit boundary condition on the *cube* surface becomes fairly insignificant. Nearer the cube, flow structure depends on the combined effect of the boundary condition on the plate and that on the cube, in a manner not easily quantified.

10. DISCUSSION

We have investigated the effect of inflow profile, momentum drag boundary conditions, and resolution, on the flow over a surface-mounted cube. With respect to the front recirculation region, we have seen that for low resolution ($N_H = 6, N_H = 8$) or for uniform flow with an ideal baseplate surface boundary condition ($\epsilon = 0$) there is no recirculation region in front of the cube. This is expected. As resolution of the flow field increases, the predicted front recirculation zone increases in length. Predicted lengths immediately in front of the cube and in the recirculation region behind the cube appear well converged at $N_H = 24$, since results for $N_H = 32$ are quite similar. Further, results for $N_H = 16$ are quite similar and are computationally much less costly. Well ahead of the cube for $N_H = 32$, there appears to be almost a “double dip” in the average velocity v_x at the base plate, suggesting the possibility that a multiple vortex system would be found in front of the cube with increasing resolution. Contour plots likewise suggest that such a weak vortex system exists. This “result” is consistent with flow visualization results of Martinuzzi and Tropea, who found the existence of such a structure in front of the cube. For resolution $N_H = 16$, in the case of uniform inflow of 3 m s^{-1} , numerical results suggest that the front recirculation length increases as the momentum deficit boundary condition becomes stronger (ϵ increases.) As ϵ increases from $\epsilon = .00005$ to $\epsilon = .0002$ and $\epsilon = .0008$ we find that the front recirculation length increases from $R_F = .35H$ to $R_F = 0.94H$ and $R_F = 1.65H$, respectively. The solution with $\epsilon = .0002$ is closest to the experimental value. For an imposed non-uniform inflow boundary layer profile, we find that the front recirculation length increases as the boundary layer thickness of the inflow profile increases. Results for which there is an ideal baseplate surface boundary condition and a moderate momentum deficit condition on the cube surface ($\epsilon = .0002$) suggest that for Case A, the thinnest boundary layer inflow, $R_F = .37H$. As the inflow boundary layer increases in thickness we find for Case B, $R_F = .96H$ and for Case C, $R_F = 1.13H$. These calculated results agree with other numerical calculations of front recirculation lengths. For example, Shah’s (1998) LES simulations for several subgrid turbulence models gave predictions of $R_F \sim 1.08H - 1.48H$. Lakehal and Rodi’s (1997) calculations for several $k - \epsilon$ models gave predictions of $R_F \sim 0.640H - 1.215H$, and they report LES simulation results of $R_F \sim 0.998H - 1.287H$. The present calculations for Case B and C inflow, and uniform inflow with $\epsilon = .0002$, also show reasonable agreement with the experimental results of Martinuzzi and Tropea (1993), who found $R_F = 1.04H$.

Investigating the recirculation region behind the cube, we encounter different trends. Here, for a uniform inflow velocity of $v_x = 3 \text{ m s}^{-1}$ and a momentum deficit surface boundary condition $\epsilon = 0.0002$, as the resolution increases, the rear circulation length decreases, and seems to converge to a fixed value, near $R_R = 2.18H$ for $N_H = 32$. We learn that there is not a monotonic trend relating the rear recirculation length R_R to ϵ , the strength of the momentum deficit boundary condition. Here for $N_H = 16$ and $\epsilon = 0$, $R_R = 2.65H$, and bounces from $R_R = 2.8H$ to $R_R = 2.52H$ and $R_R = 2.56H$ as ϵ is increased through $\epsilon = .00005, .0002$ and $.0008$. For non-uniform inflow Cases A-C, we learn that as the inflow boundary layer thickness increases, the rear recirculation length decreases and appears to be converging to a fixed value closer to accepted experimental results. For Case A, the smallest boundary layer thickness, we calculate $R_R = 2.59H$, which decreases to $R_R = 1.84H$ and $1.71H$ for Cases B and C. Present results for Case B and C inflow show the best agreement with the experimental work of Martinuzzi and Tropea (1993), who found $R_R = 1.61H$. Case B and C results are also reasonably comparable with LES results of Shah, who found $R_R \sim 1.50H - 1.69H$, and LES results of Lakehal and Rodi, who report $R_R \sim 1.432H - 1.696H$. In contrast, Lakehal and Rodi’s numerical calculations for various $k - \epsilon$ models suggest lengths $R_R \sim 2.182H - 3.405H$.

Results may also be summarized in terms of the structure of the horseshoe vortex. For uniform inflow and an ideal boundary condition on the baseplate surface, there is no recirculation region in front of the cube and so no fully formed horseshoe vortex appears there, although a strong arm-like structure does exist downstream. When a momentum deficit condition is applied at the base plate and flow is uniform, we do see recirculation in front of the cube and thus a full horseshoe vortex. However, this vortex becomes rather weak several cube lengths downstream of the cube center. For the case of non-uniform inflow of the boundary layer type given in Eq. 6, a fully formed horseshoe vortex results, the width of which becomes larger as the boundary layer thickness increases. For non-uniform flow the front portion of the horseshoe is much smoother than for the case of uniform flow. We see here the same phenomena of the downstream arms of the horseshoe becoming weaker and narrower downstream when an appreciable non-zero momentum deficit boundary condition is assigned on the base plate. Also, we note the interesting feature that for non-uniform velocity profiles, we see almost a “double arm” structure of the horseshoe far downstream. The primary arms of the horseshoe vortex are lower and further apart compared to the case of uniform flow, but several cube lengths downstream of the cube center an additional recirculation-type region seems to appear inside of the primary horseshoe arms, in a location comparable to that where the arms occur for uniform flow.

Finally, we summarize results in terms of calculated tracer concentration profiles and their comparison with the experimental data of Snyder (Zhang et al. 1996). For computed concentrations plotted transverse to the flow direction at $6.5H$ downstream, along the centerline at the baseplate behind the cube, and vertical to the baseplate at $6.5H$ downstream, we find that results for $N_H = 16, 24$, and 32 , and in some regions $N_H = 12$, are fairly comparable. For uniform flow $v_x = 3 \text{ m s}^{-1}$ and large values of ϵ , the contaminant tends to remain clustered near the back edge of the cube, so that concentrations along the baseplate centerline near the cube become higher as ϵ is increased. Smaller values of ϵ are more conducive to spreading of the contaminant in the flow field. Thus contaminant concentration profiles further downstream and lateral to the baseplate are wider and of larger magnitude as ϵ is decreased. When non-uniform inflow velocity profiles of the form given by Eq. 6 are considered, we find that for the narrowest boundary layer profile Case A, the concentration profile is wider near the back edge of the cube than concentration profiles for the thicker boundary layer inflows Cases B and C, and relatively narrower further downstream. The computed lateral concentration profiles at the baseplate $6.5H$ downstream of the cube center show that, as thickness of the inflow profile increases, the concentration profiles become wider. For Cases A, B, and C we note, however, that average concentrations at $x \sim 6.5H$, $z \sim 0$ vertical to the baseplate are all comparable, and slightly higher than the experimental range.

To investigate the importance of time-variation to the solution average, we calculate averages over several separate intervals of the time domain, and compute the standard deviation of averaged solutions. In Figure 17, averages over segments of the overall time interval are displayed for the non-uniform inflow Case B. Here averages were computed over subsets of 10,000 timesteps, with data taken every 100th timestep. Thus each average represents 100 data points in time. Much variation occurs in these averages, with peak levels of concentration both falling and rising fairly significantly as time progresses. This figure suggests that at a given point in the flow field the concentration varies significantly in time and depends intrinsically on unsteady flow physics. This suggests that data taken from too small of a time interval will provide misleading information about average characteristics.

The large time-variation in concentration profiles downstream of the cube is further illustrated by Figure 18. Here normalized concentration is plotted along with concentration levels that are one standard deviation away from the mean. The standard deviation σ is a measure of the variation of the (time-dependent) simulation data (here denoted c), and is defined as the square root of the variance σ^2 , where

$$\sigma^2 = \frac{1}{n} \sum_{i=1}^n (c_i - c_{avr})^2 = \left(\frac{1}{n} \sum_{i=1}^n c_i^2 \right) - (c_{avr})^2. \quad (7)$$

Except for near the domain edges, the magnitude of the standard deviation is comparable to that of the normalized concentration itself. This again suggests that concentration levels in the flow field are highly time-dependent. Time sequences of cross-sections (computer movies) show these fluctuations to be related to episodic vortex shedding occurring intermittently and traveling at relatively large angles to the centerline. These intermittent, episodic events also influence the contaminant tracer spreading.

11. CONCLUSIONS

Resolution, the magnitude of surface drag, and the form of the inflow velocity all affect the characteristics of flow around a surface-mounted cube. In trying to determine what set of computational parameters "best" approximates the experimental data of Castro and Robins (1977) and Snyder (Zhang et al. 1996), there is no clear answer. This is an indication that something is still missing, likely involving impressed fluctuations in the thin inflow boundary layer at the plate. When we consider average velocity profiles (v_x, v_y, v_z) downstream of the cube, the simplest case of uniform velocity, $\epsilon = 0$ best matches the experimental results of Castro and Robins. However, these conditions result in the complete absence of a recirculation region in front of the cube. The use of a non-uniform inflow velocity profile with $\epsilon = 0$ on the baseplate results in front and rear recirculation zones which agree better with experimental results, and fully formed horseshoe vortices both upstream and downstream of the cube. However, here there is a noticeable difference between the location and nature of the time-averaged horseshoe arms downstream as compared to experimental results and to the uniform inflow computed results. Calculations of tracer species concentration in subintervals of the time domain show the importance of considering time-dependent effects in order to correctly predict dispersion patterns about the cube.

It is clear that adding a dynamic spectrum of fluctuations to the inflow and boundary conditions will have some effect but this cannot yet be done with any confidence for any but channel flow experiments where the top of the channel is reasonably close to the top of the cube. This has been the subject of our current research of atmospheric wind models. A study of velocity fluctuations in the inflow profile were, therefore, excluded from the present work. Probable effects of such unsteadiness include a shortening of the calculated recirculation zone, a corresponding increase in the release rate of tracer trapped in the cube recirculation zone, and a reduced coherence of shed vortices downstream as the small scales of the impressed turbulence reinforces the natural turbulent cascade occurring anyway. An "optimization" of numerical flow parameters when modeling turbulent inflows should therefore consider these types of effects, as well as the parameters treated in detail here: numerical resolution, realistic boundary drag, and time-averaged vertical flow profiles. Differences between the present numerical results and results from experiments and other numerical calculations may in part be attributable to the different media (water versus air) and geometries (channel heights/tank dimensions) considered as well as inflow turbulence differences. We have seen that the flow around a surface-mounted cube is sensitive to both the form of the velocity upstream as well as to conditions at the baseplate surface. Furthermore, time-dependent effects are crucial to the accumulation of accurate flow field statistics and thus a correct understanding of flow and dispersion patterns, even when the inflow is steady.

12. ACKNOWLEDGEMENTS

This work was supported by the Office of Naval Research through NRL, by DARPA, and by generous grants of computer time from the DoD High Performance Computing Program Office through a National Grand Challenge Grant. The authors would like to thank Fernando Grinstein, Gopal Patnaik, and Christer Fureby for helpful comments.

12. REFERENCES

- Boris, J. P., and Book, D. L. (1973) Flux-Corrected Transport I: SHASTA – A Fluid Transport Algorithm that Works. *Journal of Computational Physics*, **11** 38-69.
- Boris, J. P., and Book, D. L. (1976) Solution of the Continuity Equation by the Method of Flux-Corrected Transport. *Methods in Computational Physics*, **16** 85-129.
- Boris, J. P., Grinstein, F. F., Oran, E. S., and Kolbe, R. L. (1992) New Insights into Large Eddy Simulation, Naval Research Laboratory Memorandum report NRL/MR/4400-92-6979.
- Boris, J. P., Landsberg, A. M., Oran, E. S., and Gardner, J. H. (1993) LCPFCT – A Flux-Corrected Transport Algorithm for Solving Generalized Continuity Equations. Naval Research Laboratory Memorandum Report NRL/MR/6410-93-7192.
- Castro, I. P. and Robins, A. G. (1977) The flow around a surface-mounted cube in uniform and turbulent streams, *Journal of Fluid Mechanics*, **79** part 2, 307-335.

- Chan, S.T., Stevens, D. E., and Lee, R. L. (2000) A Model for Flow and Dispersion around Buildings and its Validation Using Laboratory Measurements. Preprints, Third Symposium on the Urban Environment, Davis, CA, American Meteorological Society, 56-57.
- Fureby, C. and Grinstein, F. F. (1999) Monotonically Integrated Large Eddy Simulation of Free Shear Flows, *AIAA Journal*, **37** No. 5, 544-556.
- Fureby, C. and Grinstein, F. F. (2000) Large Eddy Simulation of High Reynolds-Number Free & Wall Bounded Flows *AIAA paper # 2000-2307, AIAA, Fluids 2000 meeting, Denver, CO.*
- Grinstein, F. F. and Fureby, C. (2002) Recent Progress on MILES for High Reynolds-Number Flows. *AIAA paper # 2002-0134, AIAA, 40th AIAA Aerospace Sciences Meeting and Exhibit, Reno, NV.*
- Hunt, J. C. R., Abell, C. J., Peterka, J. A., and Woo, H. (1978) Kinematical studies of the flows around free or surface-mounted obstacles; applying topology to flow visualization, *Journal of Fluid Mechanics*, **86** part 1, 179-200.
- Ikeda, T. and Nakagawa T. (1979) On the SHASTA FCT Algorithm for the Equation $\frac{\partial \rho}{\partial t} + \frac{\partial}{\partial x}(v(\rho)\rho) = 0$, *Mathematics of Computation*, **33**(148) 1157-116.
- Lakehal, D. and Rodi, W. (1997) Calculation of the flow past a surface-mounted cube with two-layer turbulence models, *Journal of Wind Eng. and Ind. Aerodynamics*, **67&68** 65-78.
- Larousse, A., Martinuzzi, R., and Tropea, C. (1993) Flow Around Surface-Mounted, Three-Dimensional Obstacles, *Turbulent Shear Flows: Selected papers from the 8th Intl. Symposium on Turbulent Shear Flows*, Durst and Friedrich, eds., Springer-Verlag, 127-139.
- Martinuzzi, R. and Tropea, C. (1993) Flow Around Surface-Mounted, Prismatic Obstacles Placed in a Fully Developed Channel Flow, *Journal of Fluids Engineering*, **115** 85-92.
- Murakami, S., Mochida, A., Hayashi, Y., and Sakamoto, S. (1992) Numerical study on velocity-pressure field and wind forces for bluff bodies by $k - \epsilon$, ASM and LES, *Journal of Wind Engineering and Industrial Aerodynamics*, **41-44** 2841-2852.
- Oran, E. S. and Boris, J. P. (2001) Numerical Simulation of Reactive Flow, Cambridge University Press, New York, Chapter 12, 443-487.
- Paterson, D. A. and Apelt, C. J. (1990) Simulation of Flow Past a Cube in a Turbulent Boundary Layer, *Journal of Wind Engineering and Industrial Aerodynamics*, **35** 149-176.
- Rodi, W., Ferziger, J. H., Breuer, M., and Pourquie, M. (1997) Status of Large Eddy Simulation: Results of a Workshop, *Journal of Fluids Engineering*, **119** 248-262.
- Shah, K. B. (1998) Large Eddy Simulation of Flow Past a Cubic Obstacle, Ph.D. Thesis, Stanford University.
- Snyder, W.H. (1994) Some observations of the influence of stratification in building wakes, *Stably Stratified Flows: Flow and Dispersion over Topography*, I.P. Castro and N.J. Rockliff, eds., Clarendon Press, 301-324.
- Tennekes, H. and Lumley, J. L. (1972) *A First Course in Turbulence*, The MIT Press, Cambridge, MA.
- Werner, H. and Wengle, H. (1993) Large-Eddy Simulations of Turbulent Flow Over and Around a Cube in a Plate Channel, *Turbulent Shear Flows: Selected papers from the 8th Intl. Symposium on Turbulent Shear Flows*, Durst and

Friedrich, eds., Springer-Verlag.

Zhang, Y. Q., Arya, S. P., and Snyder, W. H. (1996) A Comparison of Numerical and Physical modeling of Stable Atmospheric Flow and Dispersion Around a Cubical Building, *Atmospheric Environment*, **30** No. 8, 1327-1345.

Zhang, Y. Q., Huber A. H., Arya, S. P. and Snyder, W. H. (1993) Numerical Simulation to determine the effects of incident wind shear and turbulence on the flow around a building, *Journal of Wind Eng. and Ind. Aerodynamics*, **46&47** 129-134.

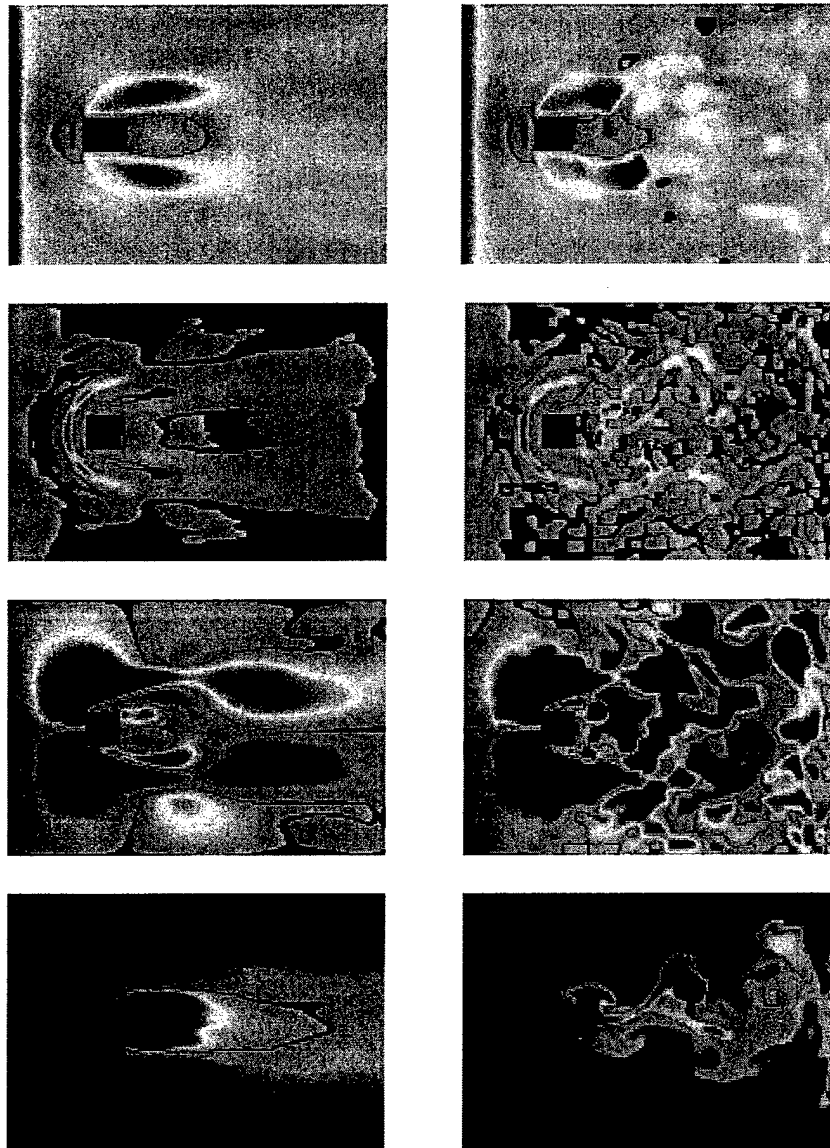


Figure 1: Time-averaged (left) and instantaneous (right) contours of velocity components v_x , v_y , and v_z and species density (top to bottom, respectively,) in a view from the top, near the baseplate.

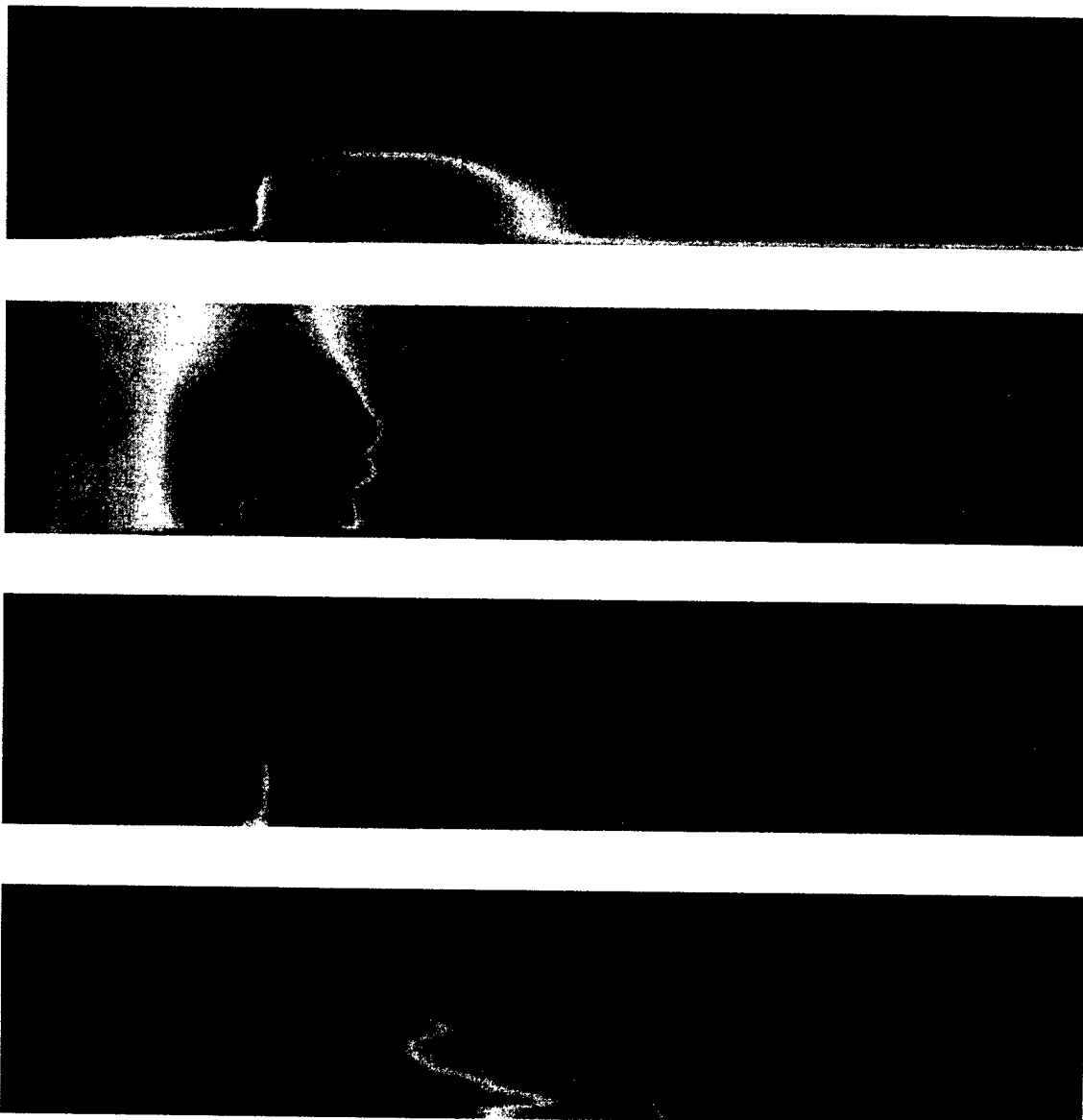


Figure 2: Time-averaged contours of velocity components v_x , v_y , v_z and species density (top to bottom, respectively.) Side view, near the longitudinal centerline.

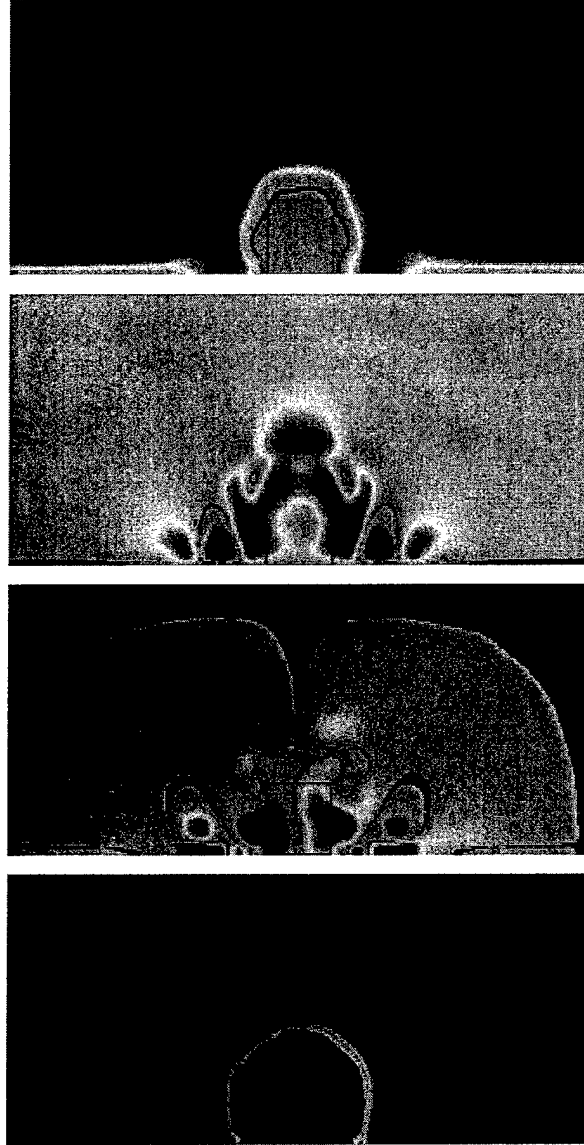


Figure 3: Time-averaged contours of velocity components v_x, v_y, v_z and species density (top to bottom, respectively.) Lateral profiles (looking streamwise), at one cube height downstream from the cube center $x \sim H$.

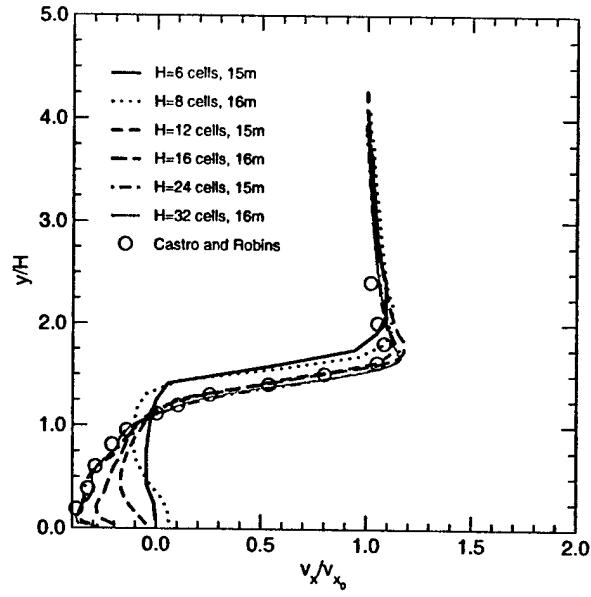


Figure 4: Average v_x velocity vertical to the baseplate, at $x \sim H, z \sim 0$, for several flow field resolutions.

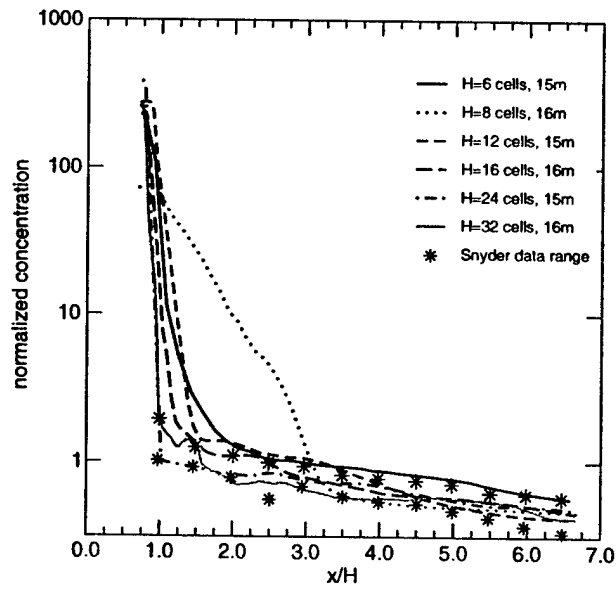


Figure 5: Normalized concentration along the baseplate centerline $y \sim 0, z \sim 0$, for several flow field resolutions.

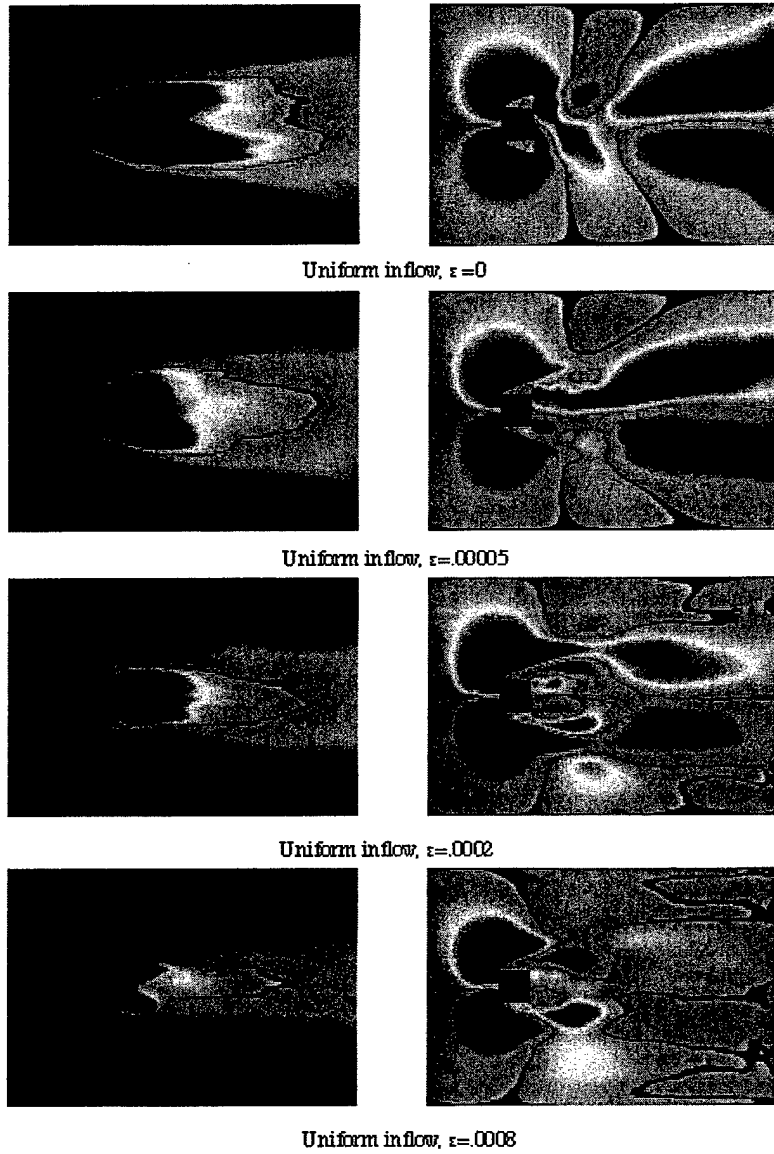


Figure 6: Contours of average concentration (left) and span-wise velocity v_z (right), top view of the baseplate surface $y \sim 0$, for several values of ϵ .

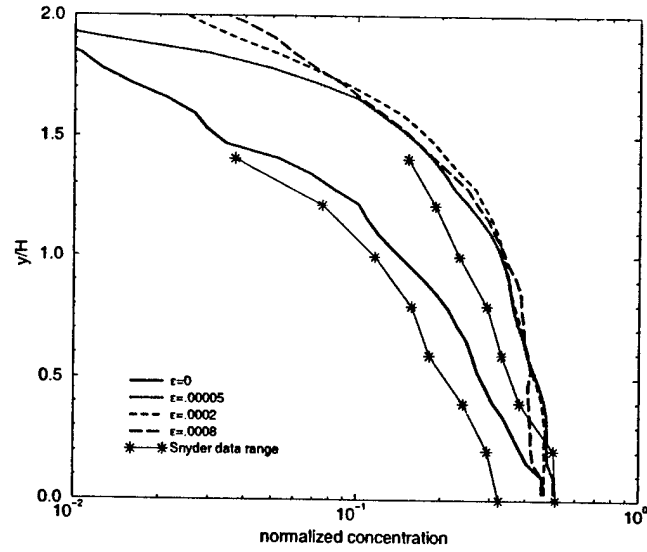


Figure 7: Average normalized concentration, at $x \sim 6.5H$, $z \sim 0$, for several values of ϵ .

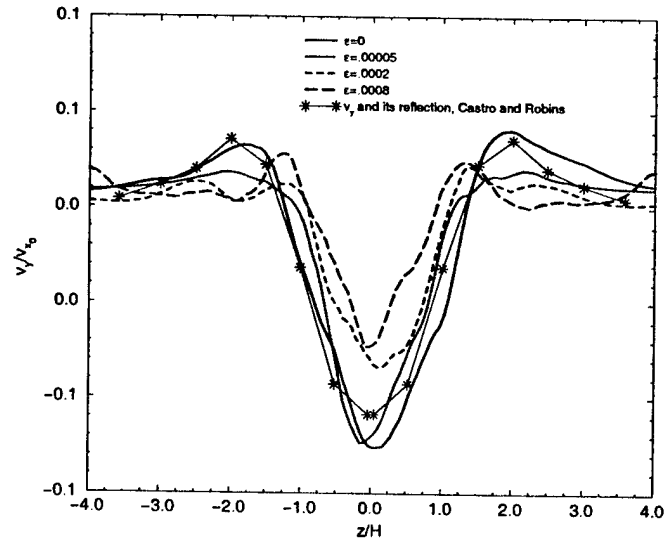


Figure 8: Average velocity v_y at $x \sim 6.5H$, $y \sim H$, for several values of ϵ .

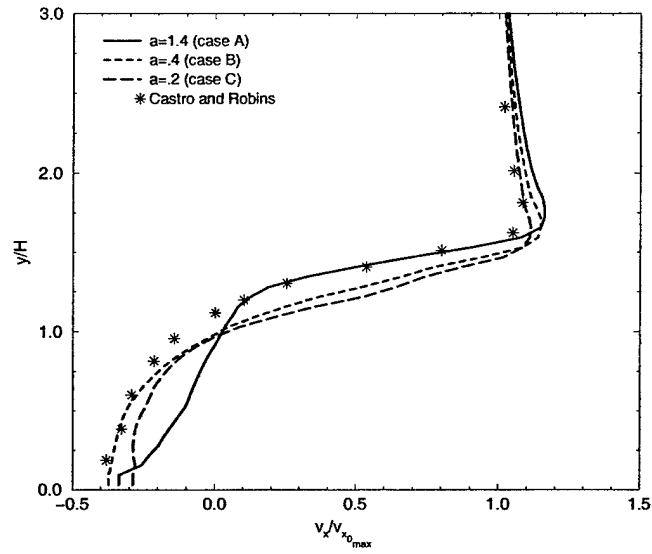


Figure 9: Average velocity v_x vertical to the baseplate at $x \sim H, z \sim 0$, for several inflow velocity profiles.

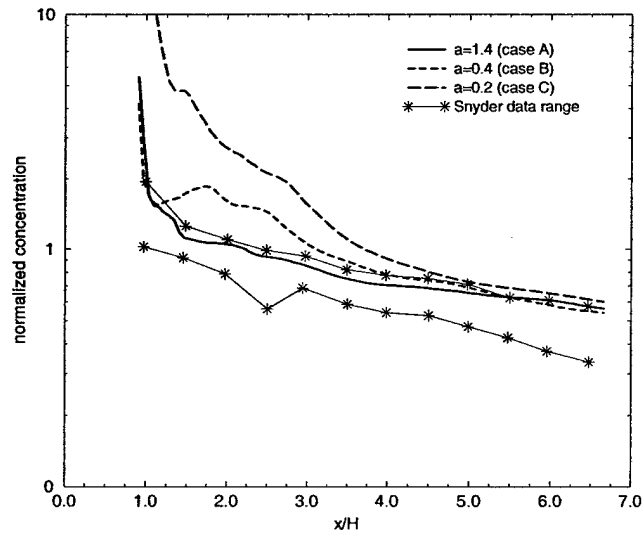
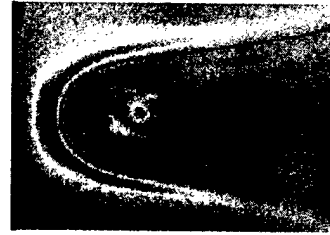


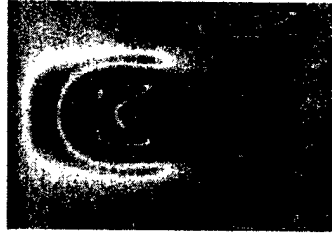
Figure 10: Average normalized concentration along the baseplate longitudinal centerline, $y \sim 0, z \sim 0$.



Uniform inflow, $\epsilon=0$ on plate and cube



Non-uniform inflow Case B, $\epsilon=0$ on plate and cube



Uniform inflow, $\epsilon=0.002$ on plate and cube



Non-uniform inflow Case B, $\epsilon=0.002$ on plate and cube

Figure 11: Contours of average velocity v_y at $y \sim 0.5H$, view from the top.

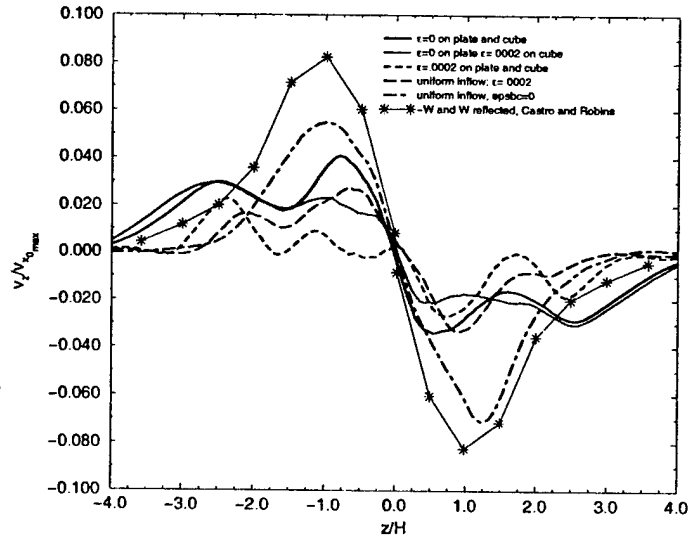


Figure 12: Average v_z velocity at $x \sim 6.5H$, $y \sim H$.

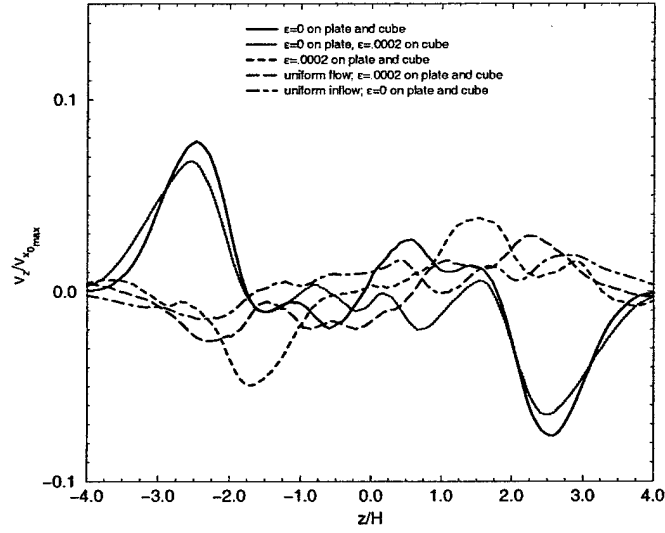


Figure 13: Average v_z velocity at $x \sim 6.5H$, $y \sim 0.5H$.

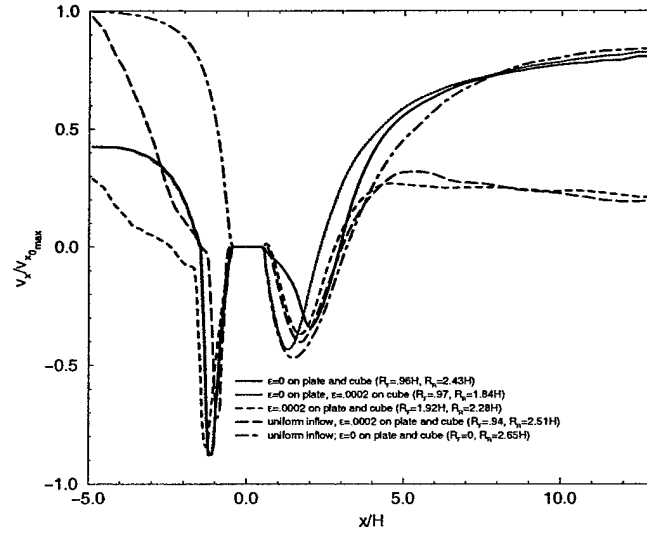


Figure 14: Average v_x velocity along the baseplate longitudinal centerline $y \sim 0$, $z \sim 0$.

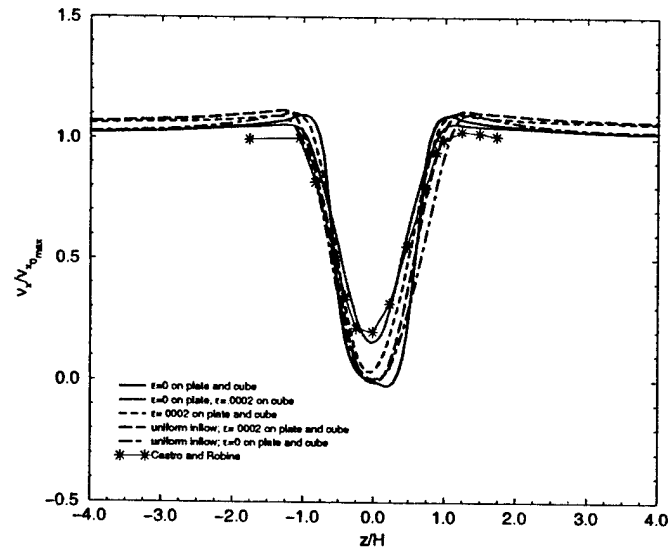


Figure 15: Average v_x velocity at $x \sim 2H, y \sim H$.

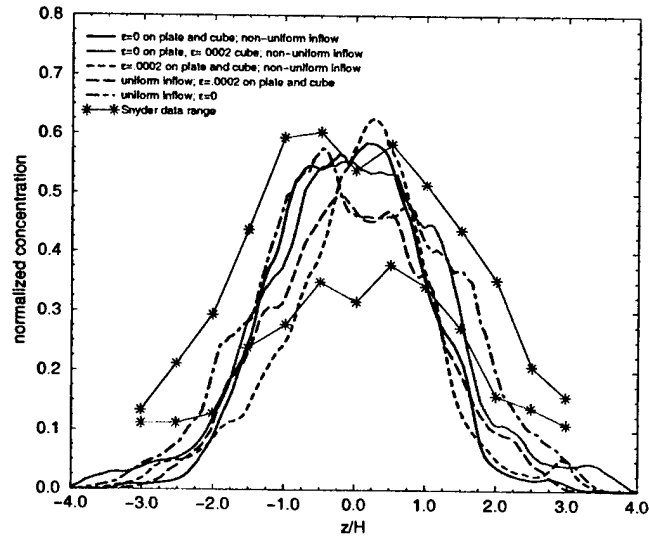


Figure 16: Average normalized concentration lateral to the baseplate, at $x \sim 6.5H, y \sim 0$.

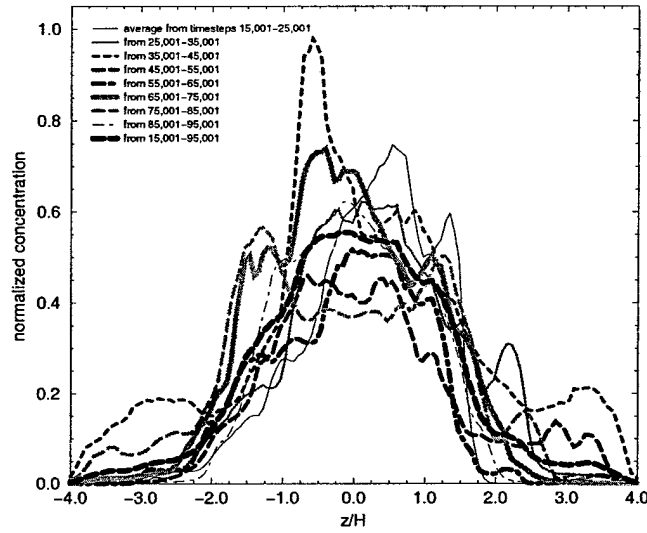


Figure 17: Average normalized concentration over several sub-intervals of the time domain; for Case B inflow with $\epsilon = 0$ on the baseplate and $\epsilon = .0002$ on the cube.

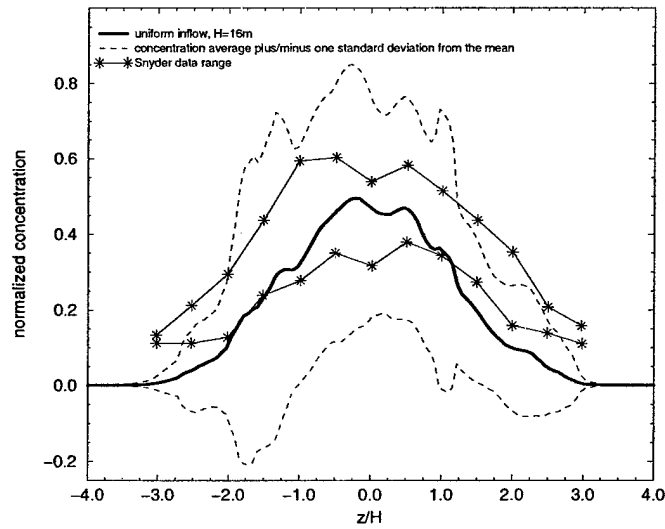


Figure 18: Average normalized concentration, and plus and minus one standard deviation, at $x \sim 6.5H, y \sim 0$. For uniform inflow, $\epsilon = .0002$.